

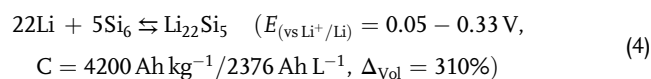
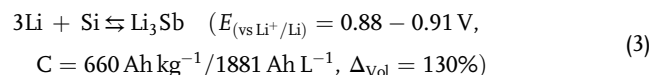
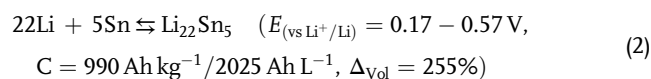
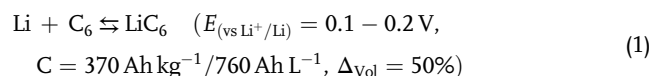
# A Li-Ion Battery Using Nanostructured Sn@C Alloying Anode and High-Voltage LiNi<sub>0.35</sub>Cu<sub>0.1</sub>Mn<sub>1.45</sub>Al<sub>0.1</sub>O<sub>4</sub> Spinel Cathode

Stanislav Levchenko, Shuangying Wei, Vittorio Marangon, and Jusef Hassoun\*

Nanostructured Sn@C anode is synthesized by carbon coating of nanosized tin for Li-ion battery. The Sn detected by X-ray diffraction (XRD) is quantified over 40 wt% by thermogravimetric analysis. Transmission and scanning electron microscopy (SEM) show a carbon matrix holding nanometric Sn operating from 0.8 to 0.01 V versus Li<sup>+</sup>/Li with low resistance, as indicated by cyclic voltammetry and electrochemical impedance spectroscopy. The Sn@C performs with initial capacity ranging from 630 mAh g<sup>-1</sup> at 200 mA g<sup>-1</sup> to 311 mAh g<sup>-1</sup> at 1200 mA g<sup>-1</sup> that decreases after 25 cycles and stabilizes to values from 403 to 268 mAh g<sup>-1</sup>, respectively. High-voltage LiNi<sub>0.35</sub>Cu<sub>0.1</sub>Mn<sub>1.45</sub>Al<sub>0.1</sub>O<sub>4</sub> cathode is achieved by coprecipitation and high-temperature treatment. XRD and SEM demonstrate the crystalline structure of the disordered spinel without impurities and homogeneous submicron morphology. Cu and Al substitution for Ni and Mn leads to excellent reversibility and low impedance, with electrochemical process evolving between 4.7 and 4.8 V versus Li<sup>+</sup>/Li. The cathode reveals a capacity of ≈110 mAh g<sup>-1</sup> retained for 88% after 100 cycles at 0.6C rate. Sn@C and LiNi<sub>0.35</sub>Cu<sub>0.1</sub>Mn<sub>1.45</sub>Al<sub>0.1</sub>O<sub>4</sub> are combined in a new Li-ion cell delivering 110 mAh g<sup>-1</sup> at 4.2 V with practical energy of 165 Wh kg<sup>-1</sup>.

their attractive features in terms of good gravimetric and volumetric energy densities (up to 250 Wh kg<sup>-1</sup> and 650 Wh L<sup>-1</sup>, respectively), absence of memory effect, and long cruise-autonomy.<sup>[2]</sup> Furthermore, the large-scale diffusion of the lithium-ion system in the global battery market has been making a steady stride toward a stage of speed development due to the rapid growth of electric vehicles (EVs) and smart power grids market.<sup>[3]</sup> Yet, the increase of the cobalt price by 2.56 times in only one and a half years (US\$ 26 500 per ton in September 2016, versus US\$ 94 250 per ton in March 2018),<sup>[4]</sup> as well as the need for improved energy density and safety content,<sup>[5]</sup> has boosted the research for new electrolytes,<sup>[6]</sup> and in particular for alternatives to the traditional LIBs electrodes, such as graphite (C<sub>6</sub>), LiCoO<sub>2</sub> (LCO), and LiNi<sub>1/3</sub>Mn<sub>1/3</sub>Co<sub>1/3</sub>O<sub>2</sub> (NMC).<sup>[7]</sup> In this scenario, a relevant breakthrough in LIBs

configuration may be achieved by replacing the commercial graphite anode by carbon composites containing various high-capacity systems, including Li-alloying metals such as Sn and Sb, or silicon.<sup>[8,9]</sup> However, a severe limit was posed by the structural instability of electrodes based on Li-alloying process, associated with the huge volume variation affecting the electrochemical reaction compared to graphite, as reported below<sup>[10]</sup>



Therefore, several Li-alloy materials have been entrapped into matrixes differing by nature and synthesis complexity, in order to achieve the structural integrity during cell operation. Among the various attempts, nanostructures containing Sn,<sup>[11,12]</sup> Sb,<sup>[13–15]</sup> and even Si<sup>[16]</sup> revealed improved performances in terms of cycle


## 1. Introduction

Lithium-ion batteries (LIBs) dominated the list over the last three decades for a wide range of consumer electronics,<sup>[1]</sup> due to

S. Levchenko, S. Wei, V. Marangon, J. Hassoun  
Department of Chemical Pharmaceutical and Agricultural Sciences  
University of Ferrara  
44121 Ferrara, Italy  
E-mail: jusef.hassoun@unife.it

J. Hassoun  
National Interuniversity Consortium of Materials Science and Technology (INSTM)  
University of Ferrara Research Unit  
University of Ferrara  
44121 Ferrara, Italy

V. Marangon, J. Hassoun  
Graphene Labs  
Istituto Italiano di Tecnologia  
16163 Genova, Italy

 The ORCID identification number(s) for the author(s) of this article can be found under <https://doi.org/10.1002/ente.202200725>.

© 2022 The Authors. Energy Technology published by Wiley-VCH GmbH. This is an open access article under the terms of the Creative Commons Attribution License, which permits use, distribution and reproduction in any medium, provided the original work is properly cited.

DOI: 10.1002/ente.202200725

life and specific capacity, despite some issue related with the synthesis complexity and scalability to achieve materials of practical interest. On the other side, many efforts have been undertaken to exploit the cobalt-free cathodes using less toxic and more abundant metals.<sup>[17,18]</sup> Among the various cobalt-free cathode materials investigated so far, spinel-structured LNMO (i.e.,  $\text{LiMn}_{0.5}\text{Ni}_{1.5}\text{O}_4$ ) has emerged as one of the most promising since their theoretical capacity of  $147 \text{ mAh g}^{-1}$  and high working potential of  $4.7 \text{ V}$  versus  $\text{Li}^+/\text{Li}$  can lead to a theoretical gravimetric energy density of about  $690 \text{ Wh kg}^{-1}$ , that is, a value approaching that of  $\text{LiNi}_{0.8}\text{Co}_{0.15}\text{Al}_{0.05}\text{O}_2$  (NCA)<sup>[19]</sup> and  $\text{LiNi}_{0.8}\text{Mn}_{0.1}\text{Co}_{0.1}\text{O}_2$  (NMC811).<sup>[20]</sup> Furthermore, advantageous characteristics including a fast lithium-ion diffusion into the 3D channels, good ionic and electronic conductivity, limited toxicity, and relevant thermal stability have been supposed to allow high power capability, modest environmental impact, and adequate safety of the cell.<sup>[21]</sup> Despite there has been a flurry of research on LNMO, the optimal performances in terms of efficiency and stability at elevated temperatures ( $>45^\circ\text{C}$ ) are still open issues.<sup>[22]</sup> Most of the above aspects affecting the reversibility of the charge/discharge processes may be related with the aggressive oxidative decomposition of conventional electrolytes at the high voltage values, the lattice modifications due to the Jahn–Teller distortion of the mixed spinel, and the possible Mn dissolution from the cathode during cycling.<sup>[23]</sup> In the most favorable case, the resultant decomposition products can form a protective layer containing both organic compounds (polyethers and carbonates) and inorganic species ( $\text{LiF}$  and  $\text{Li}_x\text{PF}_y\text{O}_z$ ) on the electrode surface, namely, a solid electrolyte interface (SEI) layer.<sup>[24]</sup> However, the SEI thickness may significantly raise during long-term cycling, thus increasing the interfacial resistance and finally hindering  $\text{Li}^+$  exchange ability.<sup>[25,26]</sup> In addition, Mn ions possibly dissolved from the LNMO cathode by traces of HF in the electrolyte can deteriorate the cathode and limit the stability of the electrode/electrolyte interface.<sup>[27]</sup> The presence of oxygen vacancies may actually affect the Ni/Mn disorder and therefore play a crucial role in the cycling stability of LNMO.<sup>[28]</sup> Moreover, possible loss of oxygen in the LNMO structure, which is observed during high-temperature synthesis (typically  $>800^\circ\text{C}$ ), can introduce secondary impurity phases such as NiO or  $\text{Li}_x\text{Ni}_{1-x}\text{O}$ .<sup>[29,30]</sup> Indeed, slight oxygen deficiency can lead to a disordered face-centered cubic spinel phase (space group  $\text{Fd}\bar{3}\text{m}$ ), while oxygen-free deficiency typically produces the ordered cubic phase (space group  $\text{P}4_3\text{32}$ ), with different cycling ability.<sup>[29]</sup> Various interesting solutions aimed to improve the cyclic behavior of the LNMO have included surface coating,<sup>[31]</sup> morphological tailoring,<sup>[32]</sup> structural disorder and lithium concentration tuning,<sup>[33,34]</sup> and partial elemental doping/substitution for Ni and/or Mn.<sup>[35–37]</sup> The latter approach has been widely considered as the most promising one to enhance the ionic and electronic conductivity, stabilize the structure, alleviate the interfacial side reactions, and improve the electrochemical properties in terms of delivered capacity, rate capability, and coulombic efficiency.<sup>[38]</sup> Most recently, single-element doping by divalent cations, such as  $\text{Cu}^{2+}$ ,  $\text{Zn}^{2+}$ , and  $\text{Mg}^{2+}$ <sup>[39–41]</sup> as well as trivalent ones, e.g.,  $\text{Al}^{3+}$ ,  $\text{Fe}^{3+}$ ,  $\text{Co}^{3+}$ , and  $\text{Cr}^{3+}$ ,<sup>[29,42,43]</sup> has been the focus of numerous research projects. Promising results have shown that partial doping or substitution by  $\text{Cu}^{2+}$  ions

could potentially improve the lithium diffusion coefficient and electronic conductivity of the LNMO due to specific outer electronic configuration of the metal.<sup>[44]</sup> The incorporation of  $\text{Cu}^{2+}$  ions may also increase the lattice parameter, lower  $\text{Li}^+$  diffusion barrier, maintain the ordered cation arrangement, thus stabilizing the cyclability, and alleviate the high voltage oxidation issue.<sup>[45,46]</sup> Aluminum was indicated as a preferable dopant and substituent owing to its high binding energy by Al–O bonds, which may suppress possible exothermic reactions, enhance the structural stability, and improve the safety content of the electrode.<sup>[47]</sup> Furthermore, substitution with electrochemically inactive metals such as Al could, in principle, buffer the disorder degree promoted by cation rearrangement during cycling, and therefore limit the formation of side phases.<sup>[48]</sup> Interestingly, the simultaneous introduction of the  $\text{Cu}^{3+}/\text{Cu}^{2+}$  redox couple and  $\text{Al}^{3+}$  ions in  $\text{LiNi}_{0.5-x}\text{Cu}_x\text{Mn}_{1.5-y}\text{Al}_y\text{O}_4$  ( $x = 0, 0.05, y = 0, 0.05$ ),<sup>[39]</sup>  $\text{LiNi}_{0.5-x}\text{Cu}_x\text{Mn}_{1.49}\text{Al}_{0.01}\text{O}_4$  ( $x = 0.01, 0.03, 0.05$ ),<sup>[49]</sup> and  $\text{LiNi}_{0.5-y}\text{Cu}_x\text{Mn}_{1.5-z}\text{Al}_x\text{O}_4$  ( $x \geq 0.1, y \geq 0.1, y + z = 2x$ )<sup>[50,51]</sup> electrodes has revealed promising performances. The multidoping strategy using  $\text{Cu}^{2+}$ ,  $\text{Al}^{3+}$ , and  $\text{Ti}^{4+}$  in  $\text{Li}[\text{Ni}_{0.455}\text{Cu}_{0.03}\text{Al}_{0.03}\text{Mn}_{1.455}\text{Ti}_{0.03}]\text{O}_4$  has shown remarkably improved cycling ability of the spinel electrode.<sup>[52]</sup> Various methods including emulsion drying,<sup>[53]</sup> ultrasonic spray pyrolysis,<sup>[54]</sup> hydrothermal,<sup>[55]</sup> sol–gel,<sup>[56]</sup> impregnation,<sup>[57]</sup> molten salt,<sup>[58]</sup> and coprecipitation<sup>[59]</sup> have been proposed as successful strategies for the synthesis of high-voltage spinel cathodes. The modified coprecipitation route appeared as a versatile approach, which can ensure simultaneous precipitating of  $\text{Li}^+$  with transition metal ions, allow easy controlling of the morphology and particle size, and large-scale production. Moreover, micro/nanostructured materials deserved special attention, particularly those obtained by a facile and mild method,<sup>[60]</sup> e.g., using oxalic acid as precipitant,<sup>[61]</sup> to achieve superior rate capability and long-life cycling performance. According to the above-described scenario on new anode and cathode materials for LIBs, we have achieved in this work a cell configuration providing the use of Li-alloying anode synthesized as a nanostructure of Sn in C, and a multi-metal spinel cathode in which Ni and Mn are partially substituted with Cu and Al, prepared by a modified coprecipitation route using ascorbic acid. This alternative system is therefore proposed as a proof-of-concept LIB for modern energy storage.

## 2. Results and Discussion

The structural and morphological features of the nanostructured Sn@C electrode synthesized in this work are reported in **Figure 1**. The X-ray diffraction (XRD) patterns of **Figure 1a** show mainly Sn in the reduced metallic state, with reflections corresponding to the tetragonal space group  $I41/amd$  (ICSD #106 072, blue pattern), without detectable signs of  $\text{SnO}_2$ . Furthermore, the predominant signal of Sn in the metal–carbon nanostructure leads to almost flat baseline significantly differing from that of the carbon matrix (red pattern), which shows instead the features of the amorphous carbon identified by broad signals centered at  $2\theta$  values of  $23^\circ$  and  $44^\circ$ .<sup>[62]</sup> Thermogravimetric analysis (TGA) performed between  $25^\circ\text{C}$  and  $1000^\circ\text{C}$  reveals the oxidation of Sn to  $\text{SnO}_2$  from  $140$  to  $380^\circ\text{C}$  with corresponding weight increase of about 5%, and the subsequent combustion

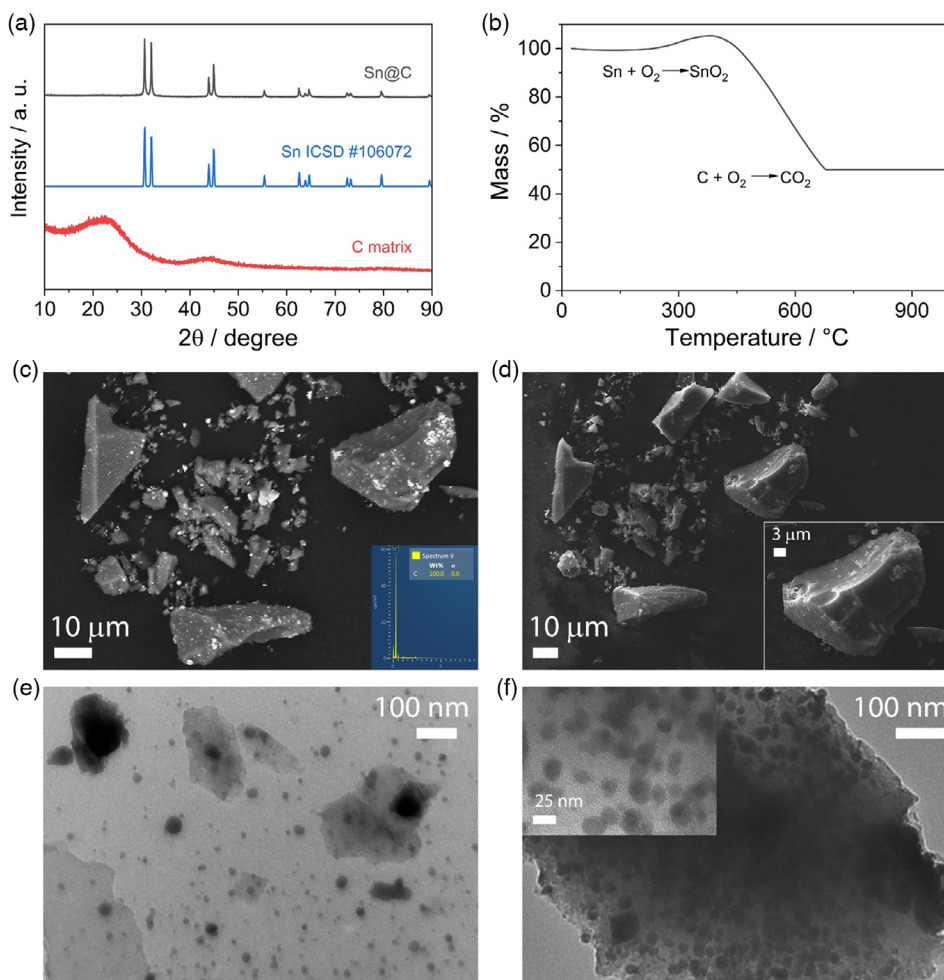


**Figure 1.** a) XRD pattern of the Sn@C sample; reference data for Sn (blue, ICSD #106 072) and experimental XRD analysis of the bare carbon matrix are reported for comparison. b) TGA performed under air flow with heating rate of  $5\text{ }^{\circ}\text{C min}^{-1}$  from 25 to  $1000\text{ }^{\circ}\text{C}$ ; inset reports the occurring reactions. SEM images of the Sn@C sample at various magnification acquired in c) BSE mode (inset shows EDS spectrum of the C matrix) and in d) SE mode (inset shows magnification). e,f) TEM images of the Sn@C sample (inset in panel f) reports higher magnification).

of C until  $680\text{ }^{\circ}\text{C}$ , thus indicating a Sn content of 40 wt% in the carbon composite. The scanning electron microscopy (SEM) image in Figure 1c recorded through the acquisition of backscattered electrons (BSE) indicates a Sn@C mainly composed of carbon particles (see EDS inset) with a size ranging from 10 to  $50\text{ }\mu\text{m}$ , occasionally hosting nanometric Sn clusters into the surface. Furthermore, the corresponding SEM recorded using secondary electrons (SE, Figure 1d) reveals only carbon (see also magnification in inset, and SEM of the C matrix reported in Figure S1, Supporting Information), thus suggesting that Sn nanoparticles are mainly located in internal shells. This hypothesis is fully verified by the transmission electron microscopy (TEM) images at various magnifications in Figure 1e,f that evidence a massive presence of spherical-like nanoparticles with a diameter from 10 to  $100\text{ nm}$  intimately hosted within the core of the amorphous carbon (see high magnification in the inset of panel f), as shown in previous paper on Sn–C nanostructures prepared using a different synthetic pathway for achieving anode materials for lithium cell applications.<sup>[11]</sup> It is worth mentioning

that the Sn located into the carbon surface may be in part oxidized in contact with air after synthesis due to its nanometric size, while the Sn hosted into the carbon bulk is more protected from oxidation.<sup>[11]</sup> On the other hand, the synthesis is designed ad hoc to avoid the complete oxidation of the Sn and to chemically reduce possible oxide formed before carbon coating by the use of an Ar–5% $\text{H}_2$  atmosphere during annealing at  $700\text{ }^{\circ}\text{C}$  (see Experimental Section for details). In addition, it may be pointed out that Sn particle size plays the most important role in determining the electrode stability. Indeed, previous works well demonstrated that anodes formed by Sn particles with size exceeding hundreds of nanometers completely fade in lithium cell until a full deactivation of the Li-alloying process due to the excessive volume variation and electrode disintegration.<sup>[63]</sup> Instead, nanostructures with Sn particles with size below 50 nanometer in the adequate carbon host almost fully hold the Li-alloying ability during cycling in lithium cell.<sup>[11]</sup>

The electrochemical process of the Sn@C electrode is investigated by coupling cyclic voltammetry (CV), electrochemical

impedance spectroscopy (EIS), and galvanostatic cycling in lithium cell, as reported in **Figure 2**. The voltammograms of Figure 2a show during the first cathodic scan a relevant broad wave ranging from 0.9 to 0.5 versus  $\text{Li}^+/\text{Li}$ , including both irreversible reduction of the electrolyte with formation of a SEI layer at the electrode surface and the formation of  $\text{Li}_x\text{Sn}$  alloy with a low  $x$  degree ( $<0.1$ ). Subsequently, the reduction proceeds with further peaks, evolving between 0.5 and 0.01 V versus  $\text{Li}^+/\text{Li}$  due to the multistep electrochemical Li–Sn-alloying process, with possible Li insertion into the amorphous carbon, until the formation of  $\text{Li}_{4.4}\text{Sn}$  and  $\text{Li}_\gamma\text{C}$  (typically with  $\gamma < 0.1$ ) at the lowest potential values.<sup>[11,12]</sup> The first anodic scan reveals various peaks between 0.2 and 0.8 V versus  $\text{Li}^+/\text{Li}$  accounting for the oxidation back and dealloying of the Li–Sn alloy to lithium and tin, as well as the deinsertion of Li from the carbon matrix. The voltammetry cycles evolve after the first scan according to the reversible Li-(de)

alloying and Li-(de)insertion processes discussed above without relevant traces of side reactions, however with a progressive decrease of the intensity due to a slight deactivation of the electrode ascribed to the partial loss of the metal fraction located at the carbon surface observed in Figure 1, which is typically induced by the excessive volume variation during the electrochemical process with consequent active material detachment.<sup>[11]</sup> The related Nyquist plots (Figure 2b) recorded by EIS at the open-circuit voltage (OCV) cell condition (see inset) and after 1, 3, 5, and 11 CV runs can be likely represented by the equivalent circuit  $R_e(R_iQ_i)Q_w$ , where  $R_e$  is the electrolyte resistance obtained as high-frequency intercept of the curve, the  $(R_iQ_i)$  elements (with  $i = 1$  or 2, depending on the state of charge) account for high–middle-frequency semicircles ascribed to the electrode/electrolyte interphase including charge transfer and SEI film resistances ( $R_i$ ) and constant phase elements (CPE  $Q_i$ ), and

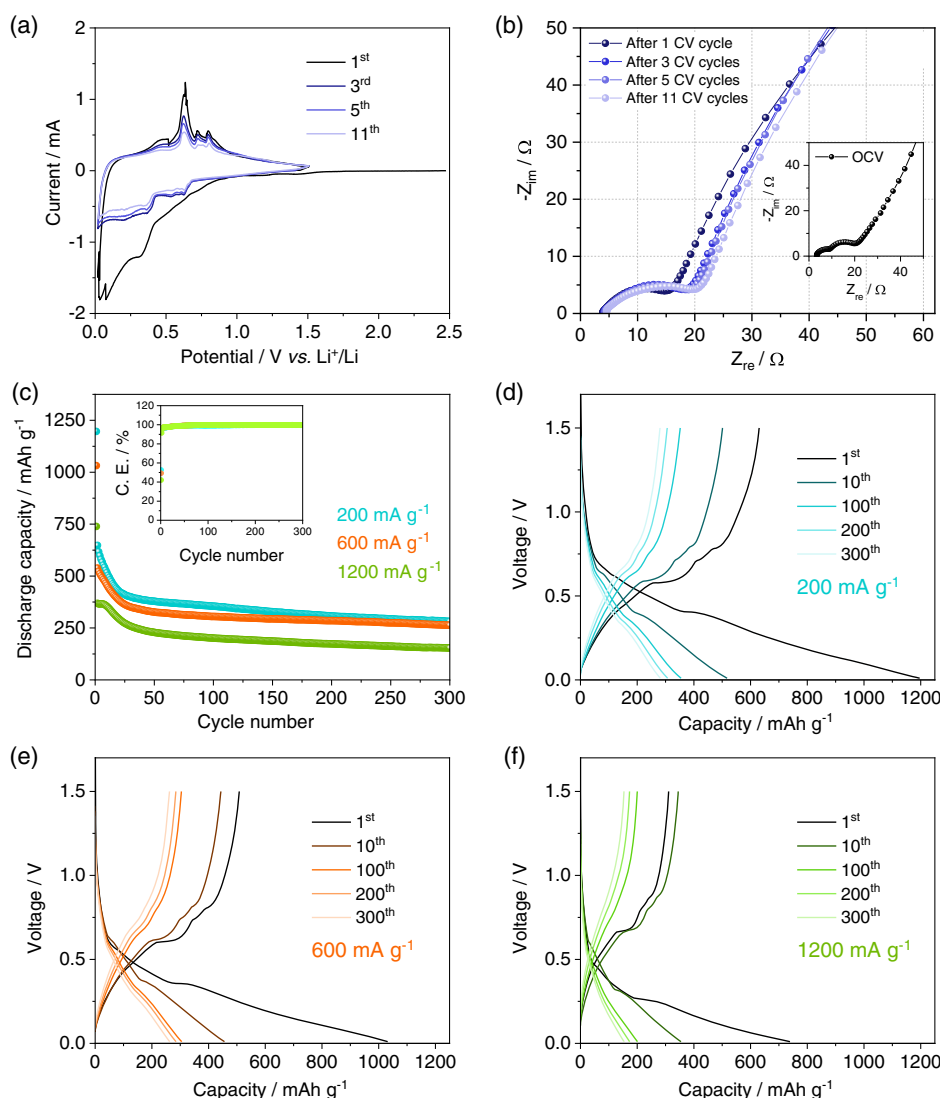


**Figure 2.** a) CV profiles and b) Nyquist plots recorded by EIS of a three-electrode  $\text{Li}|\text{Sn}@\text{C}$  half-cell; CV potential range: 0.01–1.5 V versus  $\text{Li}^+/\text{Li}$ ; CV scan rate:  $0.1 \text{ mV s}^{-1}$ ; EIS performed at the OCV condition (inset) and after 1, 3, 5, and 11 voltammetry cycles in the 500 kHz–100 MHz frequency range through an alternate voltage signal of 10 mV. c) Cycling trend (inset shows corresponding coulombic efficiency) and voltage profiles of galvanostatic cycling measurements performed at d)  $200 \text{ mA g}^{-1}$ , e)  $600 \text{ mA g}^{-1}$ , and f)  $1200 \text{ mA g}^{-1}$  current rates on  $\text{Li}|\text{Sn}@\text{C}$  half-cells; voltage range: 0.01–1.5 V.

$Q_w$  is a low-frequency CPE related to the semi-infinite length Warburg diffusion (see scheme in Figure S2, Supporting Information).<sup>[64]</sup> The plots are analyzed using the nonlinear least square (NLLS) method and the obtained results are reported in **Table 1** in terms of resistance and  $\chi^2$  accuracy, which is considered suitable at values of the order or lower than  $10^{-4}$ .<sup>[65,66]</sup> The interface resistance falls from 16.2  $\Omega$  at the OCV to 12.3  $\Omega$  after the first voltammetry cycle, due to the initial lithiation of anodic material with conductivity increase, and then slowly increases to reach 17.6  $\Omega$  after 11 CV scans due to the formation of the SEI at the electrode/electrolyte interphase.<sup>[64]</sup> The material is then cycled as the working electrode in lithium half-cell operating at current increasing from 200  $\text{mA g}^{-1}$  to a value as high as 1200  $\text{mA g}^{-1}$ . The comparison of the corresponding trends reported in Figure 2c reveals a relevant irreversible capacity during the first discharge (Li-alloying)/charge (Li-dealloying) cycle, with a low coulombic efficiency (see inset), that is, of about 53, 49, and 43% at 200, 600, and 1200  $\text{mA g}^{-1}$ , respectively. This behavior can be ascribed to side processes such as the electrolyte reductive decomposition that typically leads to SEI formation in agreement with the above-discussed CV (Figure 2a). It is worth mentioning that the first cycle (voltage profiles in Figure 2d–f) evolves with an average working voltage of 0.5 V and a high reversible capacity related to the Li-dealloying process (charge), that is, of about 630, 508, and 311  $\text{mAh g}^{-1}$  at 200, 600, and 1200  $\text{mA g}^{-1}$ , respectively. Notably, the observed capacity is higher at 200 and 600  $\text{mA g}^{-1}$  currents and lower at 1200  $\text{mA g}^{-1}$  with respect to the value estimated for the Sn@C composite taking into account 1) the contribution to the Li-insertion process related to the carbon matrix of 228, 163, and 117  $\text{mAh g}^{-1}$  at 200, 600, and 1200  $\text{mA g}^{-1}$  suggested by the corresponding cycling test in Figure S3, Supporting Information, 2) the theoretical capacity of Li–Sn-alloying process (i.e., 993  $\text{mAh g}^{-1}$ ), and 3) the tin to carbon weight ratio calculated above (i.e., 40:60 by the TGA in Figure 1b). A capacity higher than the expected one may be ascribed to a more relevant contribution of the carbon to the electrochemical process promoted by the presence of the metallic tin into the composite. Subsequently, the efficiency rapidly increases to approach 100% after the initial stages; however, the delivered capacity gradually decreases in agreement with the CV curves, due to the deactivation of the fraction of Sn hosted into the composite surface, and stabilizes upon 25 cycles to values of 403, 357, and 268  $\text{mAh g}^{-1}$  (i.e., 76, 72, and 58% of the expected value) at 200, 600, and 1200  $\text{mA g}^{-1}$ , respectively. Nevertheless, the initial decay suggests the necessity of a more optimized synthesis setup in order to achieve better performances. Indeed, techniques involving

ultrasonication for optimal dispersion coupled with a solvothermal pathway can uniformly precoat the nanometric metal particles before annealing process, thus leading to their better distribution into the carbon matrix of the final Sn@C anode as already shown by the literature paper.<sup>[67]</sup>

Crystal structure and morphology of the  $\text{LiNi}_{0.35}\text{Cu}_{0.1}\text{Mn}_{1.45}\text{Al}_{0.1}\text{O}_4$  cathode are thoroughly investigated by Rietveld refinement of the corresponding XRD data and by SEM-energy-dispersive X-ray spectroscopy (SEM-EDS) as reported in **Figure 3**. All the diffraction peaks in Figure 3a can be ascribed to the disordered  $\text{LiMn}_{1.5}\text{Ni}_{0.5}\text{O}_4$  (PDF # 80-2162) cubic face-centered spinel structure belonging to the  $\text{Fd}\bar{3}m$  (227) space group without signs of impurities related to additional metal compounds, thus suggesting the double substitutions with Cu and Al for Ni and Mn as efficient pathway to prevent the formation of side phase such as the  $\text{Li}_x\text{Ni}_{1-x}\text{O}$  one typically observed in the spinel-structured materials.<sup>[68]</sup> The figure also shows a  $I_{(311)}/I_{(400)}$  ratio of 1.01 that usually indicates an excellent stability of the  $\text{LiNi}_{0.35}\text{Cu}_{0.1}\text{Mn}_{1.45}\text{Al}_{0.1}\text{O}_4$  spinel structure, while the remarkably modest width at half-maximum (FWHM) of the peaks accounts for the relevant crystallinity of the sample.<sup>[69]</sup> Indeed, the refined structural parameters presented in **Table 2** reveal a crystallite size of about 350 nm, and a substantial agreement between the experimental pattern and the computed result due to a weighted profile factor ( $R_{\text{wp}}\%$ ) around 14% and a goodness of fit (GOF,  $\sigma$ ) of 2.0.<sup>[64,69]</sup> The controllable morphology and size, and the uniform particle distribution may actually allow a stable electrode/electrolyte interphase and favor the electrochemical performance of the material in lithium cell.<sup>[70]</sup> Therefore, the morphological features of the  $\text{LiNi}_{0.35}\text{Cu}_{0.1}\text{Mn}_{1.45}\text{Al}_{0.1}\text{O}_4$  sample are examined by SEM, while the elemental distribution and stoichiometry of the specimen are detected by SEM-EDS (Figure 3b–i). The SEM reveals a sample formed by aggregates with a size extended to tens of micrometers (Figure 3b) of interconnected nanometric primary particles ranging from 100 to 500 nm (Figure 3c), within a hierarchical micro/nanostructure. Moreover, the corresponding EDS mappings (Figure 3d–h) depict a uniform distribution of the expected elements, i.e., O, Ni, Cu, Mn, and Al, thus consisting with the XRD results. Relevantly, the atomic ratios of Ni, Cu, Mn, and Al estimated from the EDS spectra (Figure 3i) closely agree with the projected ratio of the metals in the sample, i.e., 0.7:0.2:2.9:0.2. It is worth noticing that the presence of nanometric primary particles observed herein can shorten the  $\text{Li}^+$  diffusion path and notably enhance the power output of the battery, while their micrometric agglomeration can actually relieve the surface adverse reaction and limit possible electrode/electrolyte interphase deterioration.<sup>[71]</sup> This morphology,

**Table 1.** NLLS analysis performed on the Nyquist plots reported in Figure 2b recorded by EIS on a Li|Sn@C half-cell upon CV (see Figure 2a). The NLLS fitting was performed by using the Boukamp software.<sup>[65,66]</sup>

Cell condition	Circuit	$R_1$ [ $\Omega$ ]	$R_2$ [ $\Omega$ ]	$R_1 + R_2$ [ $\Omega$ ]	$\chi^2$
OCV	$R_e(R_1Q_1)(R_2Q_2)Q_w$	6.0 $\pm$ 0.3	10.3 $\pm$ 0.4	16.3 $\pm$ 0.7	3 $\times$ 10 <sup>-4</sup>
After 1 CV run	$R_e(R_1Q_1)Q_w$	12.3 $\pm$ 0.3	/	12.3 $\pm$ 0.3	4 $\times$ 10 <sup>-4</sup>
After 3 CV runs	$R_e(R_1Q_1)Q_w$	15.8 $\pm$ 0.4	/	15.8 $\pm$ 0.4	5 $\times$ 10 <sup>-4</sup>
After 5 CV runs	$R_e(R_1Q_1)Q_w$	16.4 $\pm$ 0.5	/	16.4 $\pm$ 0.5	9 $\times$ 10 <sup>-4</sup>
After 11 CV runs	$R_e(R_1Q_1)Q_w$	17.6 $\pm$ 0.4	/	17.6 $\pm$ 0.4	5 $\times$ 10 <sup>-4</sup>

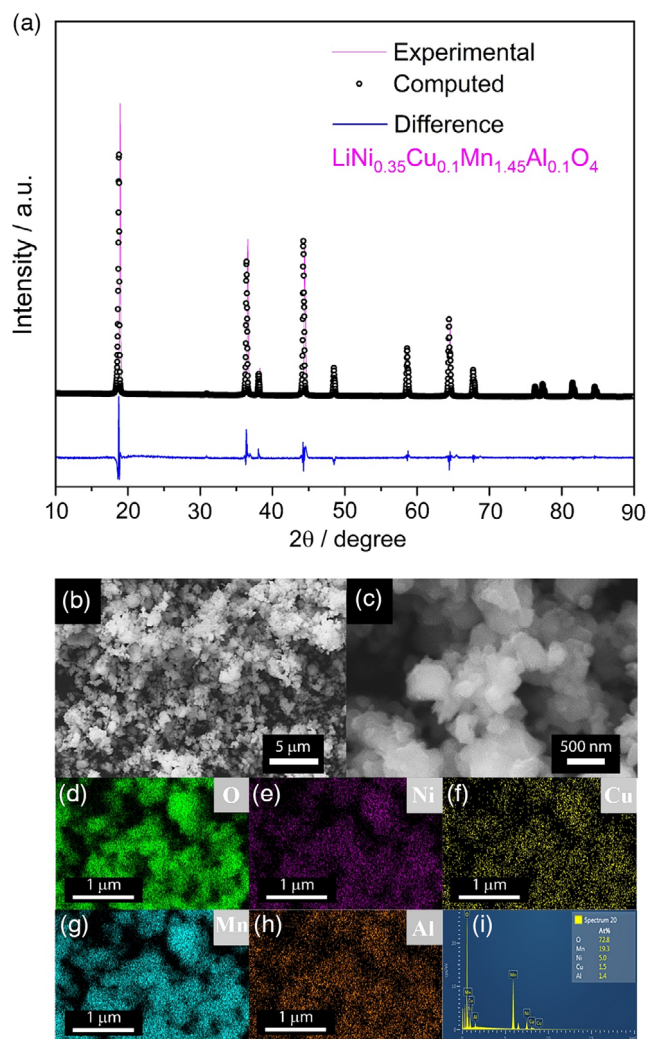


**Figure 3.** a) XRD pattern of the  $\text{LiNi}_{0.35}\text{Cu}_{0.1}\text{Mn}_{1.45}\text{Al}_{0.1}\text{O}_4$  sample (magenta line) and corresponding Rietveld refinement (dots indicate the computed pattern; blue line represents the difference between experimental and computed patterns); the pattern is indexed to the  $\text{LiNi}_{0.5}\text{Mn}_{1.5}\text{O}_4$  phase (PDF # 80-2162) with space group  $\text{Fd}\bar{3}\text{m}$  (227) (see Table 2 for the Rietveld refinement results). SEM-EDS analyses of the  $\text{LiNi}_{0.35}\text{Cu}_{0.1}\text{Mn}_{1.45}\text{Al}_{0.1}\text{O}_4$  sample, in particular: b,c) SEM images at different magnifications; EDS elemental maps of d) O, e) Ni, f) Cu, g) Mn, and h) Al; panel i) shows the EDS spectrum.

**Table 2.** Rietveld refinement analysis performed on the XRD pattern of the  $\text{LiNi}_{0.35}\text{Cu}_{0.1}\text{Mn}_{1.45}\text{Al}_{0.1}\text{O}_4$  sample (see Figure 3a) in terms of crystallite size, lattice parameters, unit cell volume, goodness-of-fit (GOF,  $\sigma$ ) parameter, and weighted-profile  $R$  factor ( $R_{\text{wp}}\%$ ).

Phase	Space group	Crystallite size [Å]	$a$ [Å]	$V$ [Å <sup>3</sup> ]	GOF [ $\sigma$ ]	$R_{\text{wp}}$ [%]
$\text{LiNi}_{0.5}\text{Mn}_{1.5}\text{O}_4$	$\text{Fd}\bar{3}\text{m}$ (#227)	$3479 \pm 0.1$	8.1740(8)	546.15(6)	2.000	14.23

as well as the defined crystalline structure and composition, is expected to promote a satisfactory cycling behavior of the  $\text{LiNi}_{0.35}\text{Cu}_{0.1}\text{Mn}_{1.45}\text{Al}_{0.1}\text{O}_4$  electrode in lithium cells.

The electrochemical response of the  $\text{LiNi}_{0.35}\text{Cu}_{0.1}\text{Mn}_{1.45}\text{Al}_{0.1}\text{O}_4$  electrode is investigated in Figure 4 by CV, EIS, and galvanostatic cycling in lithium half-cell within the voltage range between 3.0 and 5.1 V. The CV (Figure 4a) reveals a first cycle characterized by two oxidation peaks at about 4.72 and 4.82 V versus  $\text{Li}^+/\text{Li}$  during the anodic scan, reversed into two reduction peaks at 4.66 and 4.74 V versus  $\text{Li}^+/\text{Li}$  during the subsequent cathodic scan, corresponding to the  $\text{Ni}^{2+}/\text{Ni}^{3+}$  and  $\text{Ni}^{3+}/\text{Ni}^{4+}$  redox couples,<sup>[72]</sup> with a remarkable reversibility likely favored by the presence of Al.<sup>[47]</sup> The curves also show at lower potential values broad reversible signals around 4.0 and 4.3 V versus  $\text{Li}^+/\text{Li}$  due to the  $\text{Mn}^{3+}/\text{Mn}^{4+}$  and  $\text{Cu}^{2+}/\text{Cu}^{3+}$  redox pairs.<sup>[49]</sup> Relevantly, the fifth voltammetry cycle displays negligible change of the redox potentials, thus accounting for the optimal kinetics of the electrochemical process likely due to the double substitution with copper and aluminum adopted herein. However, the CV also shows a decrease of the peak intensity by the ongoing of the test and suggests a partial deactivation of the material. To shed further light on the  $\text{LiNi}_{0.35}\text{Cu}_{0.1}\text{Mn}_{1.45}\text{Al}_{0.1}\text{O}_4$  electrode/electrolyte interphase characteristics, EIS has been performed at the OCV and upon CV (Figure 4b), and the resulting Nyquist plots analyzed through NLLS method with outcomes reported in Table 3.<sup>[65,66]</sup> Indeed, the Nyquist plots at the OCV and after 5 CV runs are generally represented by the same equivalent circuit used for the  $\text{Li}|\text{Sn}@\text{C}$  cell after CV, i.e.,  $R_e(R_iQ_i)Q_w$  (see Scheme in Figure S2, Supporting Information), where  $R_e$  indicates the electrolyte resistance determined as the curve intercept at high frequency,  $(R_iQ_i)$  accounts for the depressed semicircle at medium–high frequencies with resistances ( $R_i$ ) and CPE ( $Q_i$ ) associated with interphase features such as SEI films and charge transfer, and  $Q_w$  represents the low-frequency pseudocapacitance sloped line.<sup>[64,69]</sup> The data show an initial resistance of 39  $\Omega$  at the OCV which slightly increases to reach a value of about 57  $\Omega$  after 5 voltammetry cycles in line with the CV data, thus further suggesting an adequate electrode/electrolyte interphase in terms of low resistance, high electronic conductivity, and possibly fast  $\text{Li}^+$  ion diffusion.<sup>[73]</sup> It is worth mentioning that intrinsic material properties such as the ionic and electronic conductivity, the  $\text{Li}^+$  transport properties, the cation disordering Jahn–Teller effect caused by  $\text{Mn}^{3+}$  ions, and the features of  $\text{Ni}^{2+}/\text{Ni}^{4+}$ ,  $\text{Mn}^{3+}/\text{Mn}^{4+}$ , and  $\text{Cu}^{2+}/\text{Cu}^{3+}$  redox centers can be actually improved by the presence of Al and by the morphological characteristics of the  $\text{LiNi}_{0.35}\text{Cu}_{0.1}\text{Mn}_{1.45}\text{Al}_{0.1}\text{O}_4$  cathode.<sup>[28,74]</sup> This consideration is well confirmed by the cycling response of the  $\text{LiNi}_{0.35}\text{Cu}_{0.1}\text{Mn}_{1.45}\text{Al}_{0.1}\text{O}_4$  electrode in lithium half-cell at various C-rates which is subsequently reported in terms of voltage profiles (Figure 4c) and capacity trend (Figure 4d). Hence, the voltage profiles reveal a reversible response in full agreement with CV, with short plateaus between 3.9 and 4.3 V involving the  $\text{Mn}^{3+}/\text{Mn}^{4+}$  and the  $\text{Cu}^{2+}/\text{Cu}^{3+}$  redox pair, and the main plateau in the 4.6–4.8 V range related to the  $\text{Ni}^{2+}/\text{Ni}^{4+}$  redox couple, without electrochemical contribution ascribed to aluminum.<sup>[75]</sup> Meanwhile, the  $\text{LiNi}_{0.35}\text{Cu}_{0.1}\text{Mn}_{1.45}\text{Al}_{0.1}\text{O}_4$  cathode appears moderately affected by the C-rate increase which leads to a modest polarization by ohmic dropping in the corresponding voltage profiles (Figure 4c) with a consequent slight capacity decrease from about 110  $\text{mAh g}^{-1}$  at C/12 to about 107, 102, 98, and 90  $\text{mAh g}^{-1}$  at C/6, C/3, C/2, and 1C rates, respectively (where 1C = 147  $\text{mA g}^{-1}$ ).

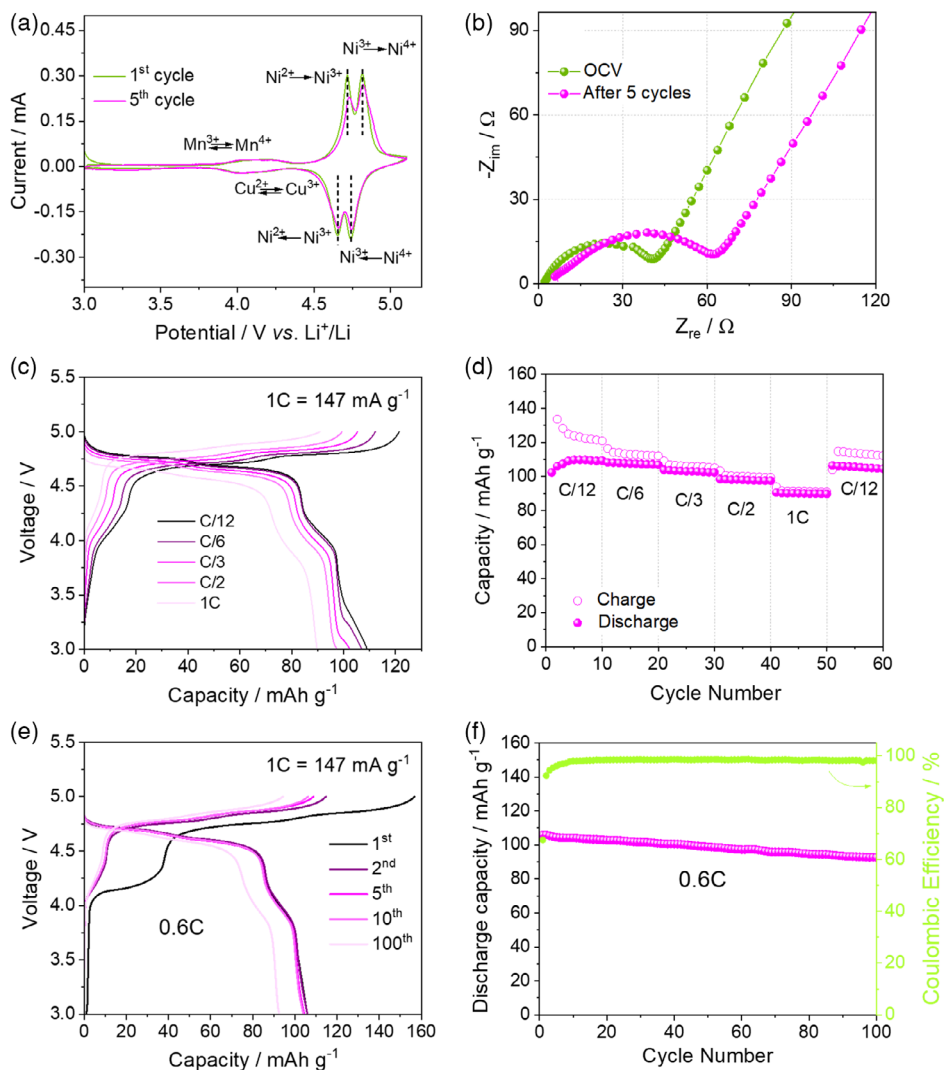


**Figure 4.** a) CV profiles and b) Nyquist plots recorded by EIS of a  $\text{LiLiNi}_{0.35}\text{Cu}_{0.1}\text{Mn}_{1.45}\text{Al}_{0.1}\text{O}_4$  half-cell; CV potential range: 3.0–5.1 V versus  $\text{Li}^+/\text{Li}$ ; scan rate:  $0.1 \text{ mV s}^{-1}$ ; EIS carried out at the OCV condition and after the fifth voltammetry cycle within the 500 kHz–100 mHz frequency range by using an alternate voltage signal of 10 mV. Rate capability carried out on a  $\text{LiLiNi}_{0.35}\text{Cu}_{0.1}\text{Mn}_{1.45}\text{Al}_{0.1}\text{O}_4$  half-cell at increasing C-rates of C/12, C/6, C/3, C/2, and 1C ( $1\text{C} = 147 \text{ mA g}^{-1}$ ) before lowering back to C/12 after 50 cycles in the 3.0–5.0 V voltage range at  $25^\circ\text{C}$  in terms of c) selected voltage profiles and d) charge/discharge capacity trend versus cycle number. Cycling response of the  $\text{LiNi}_{0.35}\text{Cu}_{0.1}\text{Mn}_{1.45}\text{Al}_{0.1}\text{O}_4$  electrode in lithium half-cell at 0.6C constant rate in the 3.0–5.0 V voltage range in terms of e) selected voltage profiles and f) capacity trend (right y-axis shows coulombic efficiency).

**Table 3.** NLLS analysis performed on the Nyquist plots reported in Figure 4b recorded by EIS on a  $\text{LiLiNi}_{0.35}\text{Cu}_{0.1}\text{Mn}_{1.45}\text{Al}_{0.1}\text{O}_4$  half-cell upon CV (see Figure 4a). The NLLS fitting method was applied by using the Boukamp software.<sup>[65,66]</sup>

Cell condition	Circuit	$R_1$ [ $\Omega$ ]	$\chi^2$
OCV	$R_e(R_1Q_1)Q_w$	$39.1 \pm 0.3$	$2 \times 10^{-4}$
After 5 CV runs	$R_e(R_1Q_1)Q_w$	$57.2 \pm 0.7$	$4 \times 10^{-4}$

However, the signatures of Figure 4d indicate a higher capacity during the charge compared to the discharge, thus suggesting a low efficiency particularly at the lowest C-rate (i.e., C/12), due to a more pronounced electrolyte oxidative decomposition at 5 V

which is kinetically favored by the modest current value. This side process can likely lead to the formation of a protective SEI layer by the ongoing of cycles.<sup>[76]</sup> Relevantly, the cell recovers almost the initial capacity of  $106 \text{ mAh g}^{-1}$  when the current is lowered back to C/12, thus accounting for the electrode stability against the stress caused by repeated current changes and for an excellent rate capability achieved by the optimal selection of chemical composition and synthesis conditions. The electrode stability is further investigated by cycling the material at the constant C-rate of 0.6C with outcomes reported in terms of voltage profiles (Figure 4e) and discharge capacity trend with coulombic efficiency (Figure 4f). The graphs depict the above-discussed signature centered at about 4.7 V and a low coulombic efficiency during the initial stages due to excessive electrolyte

decomposition, increasing from 68% during the first cycle to values exceeding 98% upon 20 cycles as the SEI layer is consolidated over the electrodes. Figure 4f also shows that the initial discharge capacity of  $106 \text{ mAh g}^{-1}$ , that is, the 72 % of the theoretical value, is relevantly retained at the 93% over 100 cycles, thus further indicating the structural stability of the  $\text{LiNi}_{0.35}\text{Cu}_{0.1}\text{Mn}_{1.45}\text{Al}_{0.1}\text{O}_4$  electrode by repeated charge/discharge process. Additional proof of cathode stability is given by Figure S4, Supporting information, which reports the galvanostatic cycling test at 0.3C rate operated at  $55^\circ\text{C}$  of the  $\text{LiNi}_{0.35}\text{Cu}_{0.1}\text{Mn}_{1.45}\text{Al}_{0.1}\text{O}_4$ . The figure shows that the presence of Cu and Al leads to a relatively low polarization of the electrochemical process (Figure S4a, Supporting Information), high coulombic efficiency during cycling after the initial stage, and an initial discharge capacity of  $110 \text{ mAh g}^{-1}$  retained for about 83% over 70 cycles. These data further account for the limitation of Mn dissolution from the spinel electrode promoted by the codoping adopted herein.

Hereafter, the applicability of the developed electrode materials is verified in the proof-of-concept Li-ion full-cell reported in Figure 5, by combining the Sn@C anode and the  $\text{LiNi}_{0.35}\text{Cu}_{0.1}\text{Mn}_{1.45}\text{Al}_{0.1}\text{O}_4$  cathode. Figure 5a depicts the comparison between the voltage profiles with respect to the areal

capacity ( $\text{mAh cm}^{-2}$ ) of the corresponding half-cells using Sn@C (red line) and  $\text{LiNi}_{0.35}\text{Cu}_{0.1}\text{Mn}_{1.45}\text{Al}_{0.1}\text{O}_4$  (blue line) during the steady state, achieved before full-cell assembly by precycling the Sn@C (see Experimental Section and Figure S5, Supporting Information), in order to evaluate the optimal N/P ratio, that is, 1.3 for the Sn@C| $\text{LiNi}_{0.35}\text{Cu}_{0.1}\text{Mn}_{1.45}\text{Al}_{0.1}\text{O}_4$  full-cell considered herein. Indeed, a full-cell without anode prelithiation would lose a relevant fraction of the cathode capacity during cycling, as the first cycle of the anode suffers from about 50% of irreversible capacity due to SEI formation as well as structural reorganization of the Li-alloying material as demonstrated by the galvanostatic cycling test of the Sn@C material in half-cell (Figure 2). Despite a better tuning of the electrolyte may alleviate this irreversible capacity by improving the SEI layer formation, the activation of the anode by electrochemical precycling or by chemical action of the lithium metal<sup>[77]</sup> certainly plays the most crucial role in ensuring the highest reversible capacity of the Sn@C and, at the same time, avoiding capacity loss during the first cycle and allowing the optimal operation in terms of the delivered capacity and cycling stability of the full Sn@C| $\text{LiNi}_{0.35}\text{Cu}_{0.1}\text{Mn}_{1.45}\text{Al}_{0.1}\text{O}_4$  cell. To further understand the practical operation, Figure 5b reports the voltage versus time trends of the full-cell cycled at the constant current rate of C/3

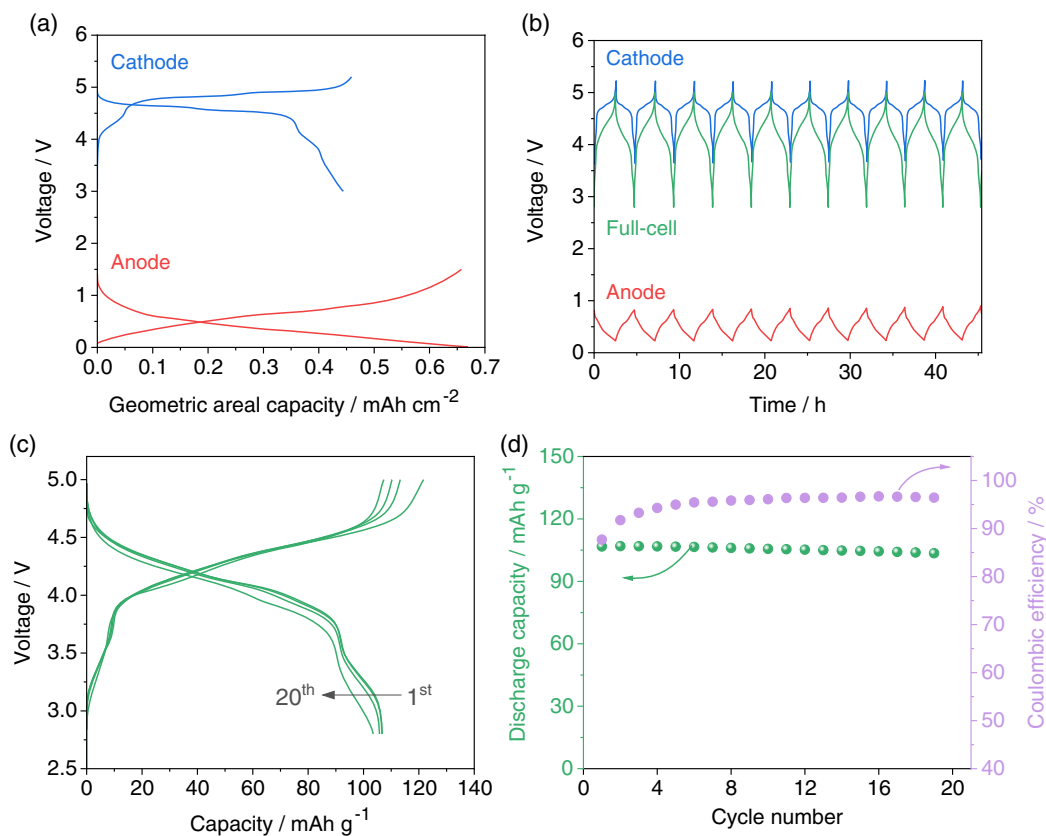


**Figure 5.** a) Comparison between voltage profiles related to Li|Sn@C (red line) and Li| $\text{LiNi}_{0.35}\text{Cu}_{0.1}\text{Mn}_{1.45}\text{Al}_{0.1}\text{O}_4$  (blue line) half-cells reported versus the corresponding geometric areal capacity ( $\text{mAh cm}^{-2}$ ) in order to evaluate the N/P ratio of the full Sn@C| $\text{LiNi}_{0.35}\text{Cu}_{0.1}\text{Mn}_{1.45}\text{Al}_{0.1}\text{O}_4$  cell; b) trends of voltage profiles versus time (hours) of Sn@C (red line) and  $\text{LiNi}_{0.35}\text{Cu}_{0.1}\text{Mn}_{1.45}\text{Al}_{0.1}\text{O}_4$  (blue line) collected using a Li reference electrode in the full Sn@C| $\text{LiNi}_{0.35}\text{Cu}_{0.1}\text{Mn}_{1.45}\text{Al}_{0.1}\text{O}_4$  cell (green line); c) voltage profiles versus gravimetric capacity ( $\text{mAh g}^{-1}$ ) and d) capacity versus cycles trend (right y-axis shows coulombic efficiency) of the full Sn@C| $\text{LiNi}_{0.35}\text{Cu}_{0.1}\text{Mn}_{1.45}\text{Al}_{0.1}\text{O}_4$  cell cycled at the constant current rate of C/3 ( $1\text{C} = 147 \text{ mA g}^{-1}$ ) between 2.8 and 5.0 V.



(1C = 147 mA g<sup>-1</sup> with respect to the cathode mass) between 2.8 and 5.0 V, in comparison with those of the Sn@C and LiNi<sub>0.35</sub>Cu<sub>0.1</sub>Mn<sub>1.45</sub>Al<sub>0.1</sub>O<sub>4</sub> as measured versus a lithium reference electrode during the test. The full-cell curve (green line) reveals a signature resulting from the combination of the sloped profile of the anode centered at an average voltage of 0.5 V (red line) and the typical spinel-cathode trend with notable symmetry evolving at high voltage mainly between 4.6 and 4.8 V (blue line). Hence, the voltage versus gravimetric capacity (mAh g<sup>-1</sup>) profiles of the Sn@C|LiNi<sub>0.35</sub>Cu<sub>0.1</sub>Mn<sub>1.45</sub>Al<sub>0.1</sub>O<sub>4</sub> battery (Figure 5c) show the abovementioned composite shape, with average working voltage of about 4.3 V and initial capacity of 110 mAh g<sup>-1</sup>, repeated without a significant shape variation upon the 20 cycles taken into consideration. Furthermore, the corresponding cycling trend (Figure 5d) indicates an initial coulombic efficiency of 88% that rapidly increases and stabilizes at 97%. The above data are considered well promising for the Sn@C|LiNi<sub>0.35</sub>Cu<sub>0.1</sub>Mn<sub>1.45</sub>Al<sub>0.1</sub>O<sub>4</sub> system. However, the full-cell may be relevantly affected by the decay experienced by the Sn@C anode during cycling that can affect the N/P ratio and alter the system balance. Side effect on the full-cell balance may be, in part, ascribed also to the possible partial electrolyte oxidation at the high voltages achieved by the LiNi<sub>0.35</sub>Cu<sub>0.1</sub>Mn<sub>1.45</sub>Al<sub>0.1</sub>O<sub>4</sub> cathode. Hence, a proper optimization of the electrolyte can also lead to the improvement of the battery cycling. Additional efforts are certainly necessary to further improve the specific values of the cell in terms of delivered capacity, efficiency, and cycle life. Despite the optimal cell balance is theoretically the unity of N/P ratio (i.e., N/P ratio = 1), the Li-ion cells are typically balanced using an excess of anode (e.g., N/P ratio = 1.05).<sup>[1]</sup> In this work, we have evaluated a N/P ratio of about 1.3 for the Sn@C|LiNi<sub>0.35</sub>Cu<sub>0.1</sub>Mn<sub>1.45</sub>Al<sub>0.1</sub>O<sub>4</sub> full-cell, and we believe that this may be further limited to values approaching 1.1 in order to ensure better cell performances. It is worth mentioning that the cell voltage and its specific capacity (referred to the cathode) shown in Figure 5 lead to a theoretical energy density approaching 500 Wh kg<sup>-1</sup>, and suggest the cell as suitable battery for possible scaling-up to achieve a new energy storage system. The above theoretical energy density value, achieved by taking into account the average cell voltage (i.e., 4.3 V), and the cathode specific capacity (i.e., 110 mAh g<sup>-1</sup>), may be reflected into a practical energy density of 165 Wh kg<sup>-1</sup> which is calculated from the cathode energy (i.e., 500 Wh kg<sup>-1</sup>), and a reduction factor of 1/3 typically adopted for the estimation of the LIBs energy density including inactive elements such as cell case and current collectors.<sup>[1]</sup> In addition to the absence of cobalt, the LIB proposed in this work can hold two further advantages. Hence, both spinel-structure cathode and Sn@C anode can deliver a notably high rate capability, thus allowing to the cell a high power density compared to the conventional LIBs. Furthermore, the two electrode materials are characterized by a good tap density which can provide a competing volumetric energy density compared to the state-of-the-art cells.<sup>[1]</sup>

### 3. Conclusions

Two electrode materials, namely, Sn@C lithium-alloying anode and LiNi<sub>0.35</sub>Cu<sub>0.1</sub>Mn<sub>1.45</sub>Al<sub>0.1</sub>O<sub>4</sub> high-voltage spinel cathode, have

been synthesized and characterized for application in a new LIB. Sn@C revealed the features of a nanostructured material formed by metal particles with size below 100 nm hosted within the micrometric carbon matrix, however with a fraction of Sn metal located in external shells. The Sn@C has shown a metal content extending over 40 wt%, and operated in lithium half-cell according to the Li-(de)alloying process below 0.8 V versus Li<sup>+</sup>/Li with limited impedance values. The cells delivered initial capacity of about 630, 508, and 311 mAh g<sup>-1</sup> at currents of 200, 600, and 1200 mA g<sup>-1</sup>, respectively, that decreased and stabilized upon 25 cycles to values above 403, 357, and 268 mAh g<sup>-1</sup> after achieving an efficiency approaching 100% upon cycling. These data indicated a good response of the Sn@C electrode at high current values due to the nanostructured feature; however, the initial decay attributed to possible loss of the Sn particles hosted beyond the carbon matrix suggested the necessity of a more optimized synthesis setup to achieve better performances. The LiNi<sub>0.35</sub>Cu<sub>0.1</sub>Mn<sub>1.45</sub>Al<sub>0.1</sub>O<sub>4</sub> has evidenced the cubic face-centered spinel structure with relevant crystallinity and stability, without impurities related to additional metal compounds such as the Li<sub>x</sub>Ni<sub>1-x</sub>O. The cathode material was formed by aggregates extended to tens of micrometers of interconnected nanosized primary particles ranging from 100 to 500 nm within a hierarchical micro/nanostructure with uniform distribution of O, Ni, Cu, Mn, and Al. The LiNi<sub>0.35</sub>Cu<sub>0.1</sub>Mn<sub>1.45</sub>Al<sub>0.1</sub>O<sub>4</sub> revealed a well reversible signature in lithium half-cell, with peaks in the interval between 4.6 and 4.9 V versus Li<sup>+</sup>/Li corresponding to the Ni<sup>2+</sup>/Ni<sup>3+</sup> and Ni<sup>3+</sup>/Ni<sup>4+</sup> redox couples, and around 4.0 and 4.3 V versus Li<sup>+</sup>/Li due to Mn<sup>3+</sup>/Mn<sup>4+</sup> and Cu<sup>2+</sup>/Cu<sup>3+</sup>, as well as a low and stable impedance. The cathode delivered a capacity from 110 mAh g<sup>-1</sup> at C/12 to about 107, 102, 98, and 90 mAh g<sup>-1</sup> at C/6, C/3, C/2, and 1C rates, respectively, with lower coulombic efficiency at the low currents compared to high ones. Furthermore, the efficiency raised to about 98% upon cycling at 0.6C as the SEI layer was consolidated over the electrodes with initial discharge capacity of 106 mAh g<sup>-1</sup> relevantly retained for 93% over 100 cycles, thus indicating a remarkable stability of the LiNi<sub>0.35</sub>Cu<sub>0.1</sub>Mn<sub>1.45</sub>Al<sub>0.1</sub>O<sub>4</sub> electrode promoted by the tuned synthesis condition and the double substitutions with Cu and Al for Ni and Mn. A full Li-ion cell coupling Sn@C and LiNi<sub>0.35</sub>Cu<sub>0.1</sub>Mn<sub>1.45</sub>Al<sub>0.1</sub>O<sub>4</sub> has been prepared and cycled at C/3, showing a composite signature resulting from the sloped profile of the anode and the symmetrical spinel-cathode trend with an average working voltage of about 4.3 V, a coulombic efficiency of 88% rapidly increasing and stabilizing at 97%, and an initial capacity of 110 mAh g<sup>-1</sup>. The data indicated a theoretical energy density approaching 500 Wh kg<sup>-1</sup> (versus cathode mass) that may lead to a practical energy density of 165 Wh kg<sup>-1</sup> and high power. It is worth mentioning that the initial capacity exceeding 500 mAh g<sup>-1</sup>, the high tap density, and the excellent rate capability of the Sn@C can potentially increase the gravimetric and volumetric energy density of the cell as well as its power density. However, the partial deactivation of the Li-alloying process by cycling actually represents an issue still to be solved. Nevertheless, the results reported herein show that this material may be employed as a negative electrode combined with the high-voltage LiNi<sub>0.35</sub>Cu<sub>0.1</sub>Mn<sub>1.45</sub>Al<sub>0.1</sub>O<sub>4</sub> spinel in a proof-of-concept full-cell in alternative to the commercially available LIBs. These promising features, along with the complete absence

of the toxic and expensive cobalt, may possibly allow the achievement of a new energy storage system upon a further improvement of the efficiency and cycle life.

## 4. Experimental Section

**Synthesis of Sn@C Material:** A 9.5 mL of distilled water was added to 0.5 g of nanometric Sn powder (<150 nm, ≥99% trace metal basis, Sigma-Aldrich) and 2.38 g of sucrose (≥99.0%, Fluka Analytical) to obtain a water to sucrose weight ratio of 8:2, and Sn to C weight ratio of 1:2. This mixture was heated in silicon bath at 50 °C, under magnetic stirring until complete evaporation of water to precipitate a dry layer of sucrose containing the nanometric tin. Afterward, the obtained solid was heated in a tube furnace at 700 °C for 3 h using a heating rate of 5 °C min<sup>-1</sup> under Ar/H<sub>2</sub> flow (5% H<sub>2</sub>) and cooled to the room temperature. The material was subsequently ground in an agate mortar to achieve a fine powder of the composite indicated with the acronym Sn@C. A carbonaceous matrix was synthesized using water/sucrose solution within the same setup described for Sn@C material and used as the reference for structure, morphology, and electrochemical response.

**Synthesis of LiNi<sub>0.35</sub>Cu<sub>0.1</sub>Mn<sub>1.45</sub>Al<sub>0.1</sub>O<sub>4</sub> Material:** The LiNi<sub>0.35</sub>Cu<sub>0.1</sub>Mn<sub>1.45</sub>Al<sub>0.1</sub>O<sub>4</sub> material was synthesized by a procedure described in a previous paper for another spinel-type electrode in which we exploited a different metal (Fe instead of Al), and developed the concept of the “multimetal” doping as a synergic strategy that leads to a notable stabilization of the cathode by the partial presence of inactive elements.<sup>69</sup> However, we neglected herein the preparation of further samples using only Al or Cu to avoid excessive limitation of the delivered capacity because Al is not active, and Cu has a partial role at the lower voltage values. LiCH<sub>3</sub>COO·2H<sub>2</sub>O (99%, Sigma-Aldrich), Ni(CH<sub>3</sub>COO)<sub>2</sub>·4H<sub>2</sub>O (99%, Sigma-Aldrich), Cu(CH<sub>3</sub>COO)<sub>2</sub>·4H<sub>2</sub>O (99%, Sigma-Aldrich), Mn(CH<sub>3</sub>COO)<sub>2</sub>·4H<sub>2</sub>O (99%, Sigma-Aldrich), and Al(NO<sub>3</sub>)<sub>3</sub>·3H<sub>2</sub>O (99%, Sigma-Aldrich) were dissolved in hydroalcoholic solution of water and ethanol (1:5 V:V) with the molar ratio of 1.1:0.35:0.1:1.45:0.1, that is, using a 10% excess lithium source with respect to the stoichiometric amounts required to achieve the LiNi<sub>0.35</sub>Cu<sub>0.1</sub>Mn<sub>1.45</sub>Al<sub>0.1</sub>O<sub>4</sub> compound. An oxalic acid solution (H<sub>2</sub>C<sub>2</sub>O<sub>4</sub>·2H<sub>2</sub>O, Sigma-Aldrich) was added dropwise to the same volume of the above metal acetate solution under constant stirring to get a pale green suspension. The above suspension was stirred for 12 h at room temperature, and overnight at 80 °C to achieve a green precipitate (i.e., M<sub>2</sub>C<sub>2</sub>O<sub>4</sub>·xH<sub>2</sub>O, where M = Li, Ni, Cu, Mn, Al) which was ground into an agate mortar, transferred to a tube furnace, and then calcinated in a dry air flow at 500 °C for 6 h using a heating rate of 5 °C min<sup>-1</sup>. The obtained oxide powder was pressed into pellets of 14 mm of diameter, subsequently calcinated at 800 °C for 12 h using a heating rate of 5 °C min<sup>-1</sup> in dry air flow, slowly cooled to room temperature, and finely ground in an agate mortar.

**Characterization:** The crystal structures of Sn@C and LiNi<sub>0.35</sub>Cu<sub>0.1</sub>Mn<sub>1.45</sub>Al<sub>0.1</sub>O<sub>4</sub> were investigated by XRD using a Bruker D8-Advance diffractometer employing a Cu K $\alpha$  radiation by scanning 2 $\theta$  from 10° to 90° with a step size of 0.02° every 10 s. The Sn@C diffraction patterns were compared to bare Sn data collected from the International Crystallographic Structures Database (ICSD) and to the diffraction patterns of the synthesized reference carbon matrix. Phase identification and crystallinity of the LiNi<sub>0.35</sub>Cu<sub>0.1</sub>Mn<sub>1.45</sub>Al<sub>0.1</sub>O<sub>4</sub> spinel were studied through the Rietveld refinement using a MAUD analysis software and the corresponding ICDS reference data.

Morphological characteristics, composition, and stoichiometry of the samples were investigated by SEM (a Zeiss EVO 40 with a LaB6 thermionic gun), SEM-EDS (a X-ACT Cambridge Instrument), and TEM (a Zeiss EM 910) with a tungsten thermionic electron gun operated at 100 kV.

The Sn content of the Sn@C material was determined through TGA, by increasing temperature from 25 to 1000 °C with heating rate of 5 °C min<sup>-1</sup> in dry air flow with a Mettler Toledo-TGA 2 instrument.

The electrodes were prepared by casting a slurry formed by dispersing the active material (either Sn@C or LiNi<sub>0.35</sub>Cu<sub>0.1</sub>Mn<sub>1.45</sub>Al<sub>0.1</sub>O<sub>4</sub>), poly

(vinylidene fluoride) (PVDF, Solef 6020), and Super P conductive carbon (Timcal) in N-methyl-2-pyrrolidone (NMP, Sigma-Aldrich), with a weight ratio of 8:1:1. The slurry was cast either on Cu foil (Sn@C) or Al foil (LiNi<sub>0.35</sub>Cu<sub>0.1</sub>Mn<sub>1.45</sub>Al<sub>0.1</sub>O<sub>4</sub>) by using a doctor blade (MTI Corporation) and subsequently dried at around 70 °C for 3 h to remove the solvent. The obtained foils were punched into disks with the area of 1.539 cm<sup>2</sup> (diameter of 14 mm) and 0.7854 cm<sup>2</sup> (diameter of 10 mm). These disks were collected and further dried overnight under high vacuum at 110 °C. The mass loading of the electrodes was between 1.5 and 3.0 mg cm<sup>-2</sup> for Sn@C, and between 3.0 and 5.5 mg cm<sup>-2</sup> for LiNi<sub>0.35</sub>Cu<sub>0.1</sub>Mn<sub>1.45</sub>Al<sub>0.1</sub>O<sub>4</sub>. CR2032 coin-type half-cells (MTI Corporation, 14 mm electrode diameter) and three-electrode T-type cells (10 mm electrode diameter) were assembled under Argon atmosphere in a glove box (MBraun, O<sub>2</sub> and H<sub>2</sub>O contents lower than 1 ppm). Lithium metal disks were used as the counter/reference electrodes in lithium half-cells, and 1 M solution (Sigma-Aldrich) of lithium hexafluorophosphate (LiPF<sub>6</sub>) in a 1:1 v:v mixture of ethylene carbonate (EC)/dimethyl carbonate (DMC) in a Whatman glass fiber (GF/A) as the separator. The electrochemical behavior of the electrodes in lithium half-cell was studied using CV and EIS in three-electrode T-type cell employing a VersaSTAT MC Princeton Applied Research (PAR) multi-channel potentiostat. CV was performed within the potential range from 0.01 to 1.5 V versus Li<sup>+</sup>/Li for Sn@C and from 3.0 to 5.1 V versus Li<sup>+</sup>/Li for LiNi<sub>0.35</sub>Cu<sub>0.1</sub>Mn<sub>1.45</sub>Al<sub>0.1</sub>O<sub>4</sub> at scan rate of 0.1 mV s<sup>-1</sup>. Impedance spectra were collected at OCV before cycling the cell and upon CV using an alternate voltage with an amplitude of 10 mV from a frequency of 500 MHz to 100 mHz. NLLS analysis was performed on the EIS spectra using a Boukamp software considering only fits with a  $\chi^2$  value of the order or lower than 10<sup>-4</sup>.<sup>[65,66]</sup>

Galvanostatic cycling tests were carried out using a MACCOR Series 4000 Battery test system. The Sn@C was cycled in T-type lithium half-cell using two-electrode configuration between 0.01 and 1.5 V at specific currents of 200, 600, and 1200 mA g<sup>-1</sup> for 300 cycles. The cycling tests of the LiNi<sub>0.35</sub>Cu<sub>0.1</sub>Mn<sub>1.45</sub>Al<sub>0.1</sub>O<sub>4</sub> electrode were conducted in CR2032 coin-type cell between 3.0 and 5.0 V at the constant C-rate of 0.6C (1C = 147 mA g<sup>-1</sup>), and by applying various C rates every 10 cycles, namely, C/12, C/6, C/3, C/2, 1C, and moving back to a rate of C/12 at the 51th cycle.

A Li-ion full-cell was assembled by coupling the Sn@C anode with the LiNi<sub>0.35</sub>Cu<sub>0.1</sub>Mn<sub>1.45</sub>Al<sub>0.1</sub>O<sub>4</sub> cathode using the same electrolyte employed for the half cells, i.e., EC:DMC 1:1 (v:v), 1M LiPF<sub>6</sub>. The system was held by a T-type configuration equipped with a lithium reference electrode in order to check the behavior of Sn@C and LiNi<sub>0.35</sub>Cu<sub>0.1</sub>Mn<sub>1.45</sub>Al<sub>0.1</sub>O<sub>4</sub> electrodes during full-cell operation. Prior to operate in the above Li-ion cell, the Sn@C electrode was activated in a half-cell using the EC:DMC 1:1 (v:v), 1M LiPF<sub>6</sub> electrolyte for 30 galvanostatic cycles at 200 mA g<sup>-1</sup> between 0.01 and 1.5 V, and a last cycle with charge limited to 0.9 V to achieve the steady-state performance (see Figure S4, Supporting Information). The Sn@C|LiNi<sub>0.35</sub>Cu<sub>0.1</sub>Mn<sub>1.45</sub>Al<sub>0.1</sub>O<sub>4</sub> battery was prepared by using a negative to positive (N/P) capacity ratio of about 1.3, determined by taking into account the maximum capacity of Sn@C (630 mAh g<sup>-1</sup>), the theoretical capacity of LiNi<sub>0.35</sub>Cu<sub>0.1</sub>Mn<sub>1.45</sub>Al<sub>0.1</sub>O<sub>4</sub> (147 mAh g<sup>-1</sup>), and their mass loadings (1.6 and 5.4 mg cm<sup>-2</sup>, respectively). The full cell was cycled at C/3 rate in the 2.8–5.0 V voltage range (where 1C was 147 mA g<sup>-1</sup> referred to the cathode mass). All the above-described cycling tests were performed at the room temperature (25 °C). An additional cycling tests of the LiNi<sub>0.35</sub>Cu<sub>0.1</sub>Mn<sub>1.45</sub>Al<sub>0.1</sub>O<sub>4</sub> in half cell was operated at 0.3C rate (1C = 147 mA g<sup>-1</sup>) in the voltage range from 3.0 to 5.0 V by increasing the temperature to 55 °C to check the electrode stability upon operating at high temperature.

## Supporting Information

Supporting Information is available from the Wiley Online Library or from the author.

## Acknowledgements

This work has received funding from the European Union's Horizon 2020 research and innovation program Graphene Flagship under grant agreement no. 881603. The authors also thank grant "Fondo di Ateneo per la Ricerca Locale (FAR) 2021," University of Ferrara, and the collaboration project "Accordo di Collaborazione Quadro 2015" between University of Ferrara (Department of Chemical and Pharmaceutical Sciences) and Sapienza University of Rome (Department of Chemistry).

Open Access Funding provided by Universita degli Studi di Ferrara within the CRUI-CARE Agreement.

## Conflict of Interest

The authors declare no conflict of interest.

## Data Availability Statement

The data that support the findings of this study are available in the supplementary material of this article.

## Keywords

high-voltage spinel, Li-alloying, Li-ion batteries,  $\text{LiNi}_{0.35}\text{Cu}_{0.1}\text{Mn}_{1.45}\text{Al}_{0.1}\text{O}_4$ , Sn@C

Received: July 6, 2022

Revised: August 17, 2022

Published online: September 22, 2022

- [1] D. Di Lecce, R. Verrelli, J. Hassoun, *Green Chem.* **2017**, *19*, 3442.
- [2] H. Yang, H. H. Wu, M. Ge, L. Li, Y. Yuan, Q. Yao, J. Chen, L. Xia, J. Zheng, Z. Chen, J. Duan, K. Kisslinger, X. C. Zeng, W. K. Lee, Q. Zhang, J. Lu, *Adv. Funct. Mater.* **2019**, *29*, 1808825.
- [3] Q. Dai, J. C. Kelly, L. Gaines, M. Wang, *Batteries* **2019**, *5*, 48.
- [4] A. Aishova, G. Park, C. S. Yoon, Y. Sun, *Adv. Mater.* **2020**, *10*, 1903179.
- [5] Y. Wu, W. Wang, J. Ming, M. Li, L. Xie, X. He, J. Wang, S. Liang, Y. Wu, *Adv. Funct. Mater.* **2019**, *29*, 1805978.
- [6] D. Di Lecce, V. Marangon, H.-G. Jung, Y. Tominaga, S. Greenbaum, J. Hassoun, *Green Chem.* **2022**, *24*, 1021.
- [7] D. Di Lecce, S. Levchenko, F. Iacoviello, D. J. L. Brett, P. R. Shearing, J. Hassoun, *ChemSusChem* **2019**, *12*, 3550.
- [8] X. Zuo, J. Zhu, P. Müller-Buschbaum, Y.-J. Cheng, *Nano Energy* **2017**, *31*, 113.
- [9] M. N. Obrovac, L. Christensen, D. B. Le, J. R. Dahn, *J. Electrochem. Soc.* **2007**, *154*, A849.
- [10] J. L. Tirado, *Mater. Sci. Eng., R* **2003**, *40*, 103.
- [11] J. Hassoun, G. Derrien, S. Panero, B. Scrosati, *Adv. Mater.* **2008**, *20*, 3169.
- [12] J. Hassoun, P. Ochal, S. Panero, G. Mulas, C. Bonatto Minella, B. Scrosati, *J. Power Sources* **2008**, *180*, 568.
- [13] J. Hassoun, G. Derrien, S. Panero, B. Scrosati, *Electrochim. Acta* **2009**, *54*, 4441.
- [14] L. Xiao, Y. Cao, J. Xiao, W. Wang, L. Kovarik, Z. Nie, J. Liu, *Chem. Commun.* **2012**, *48*, 3321.
- [15] J. Hassoun, G. Derrien, S. Panero, B. Scrosati, *J. Power Sources* **2008**, *183*, 339.
- [16] C. Kim, M. Ko, S. Yoo, S. Chae, S. Choi, E.-H. Lee, S. Ko, S.-Y. Lee, J. Cho, S. Park, *Nanoscale* **2014**, *6*, 10604.
- [17] L. Mu, W. H. Kan, C. Kuai, Z. Yang, L. Li, C. J. Sun, S. Sainio, M. Avdeev, D. Nordlund, F. Lin, *ACS Appl. Mater. Interfaces* **2020**, *12*, 12874.
- [18] J. Abou-Rjeily, I. Bezza, N. A. Laziz, C. Autret-Lambert, M. T. Sougrati, F. Chamouss, *Energy Storage Mater.* **2020**, *26*, 423.
- [19] Y. Nie, W. Xiao, C. Miao, M. Xu, C. Wang, *Electrochim. Acta* **2020**, *334*, 135654.
- [20] F. Xin, H. Zhou, X. Chen, M. Zuba, N. Chernova, G. Zhou, M. S. Whittingham, *ACS Appl. Mater. Interfaces* **2019**, *11*, 34889.
- [21] N. Kiziltas-Yavuz, M. Yavuz, S. Indris, N. N. Bramnik, M. Knapp, O. Dolotko, B. Das, H. Ehrenberg, A. Bhaskar, *J. Power Sources* **2016**, *327*, 507.
- [22] H. Sun, B. Xia, W. Liu, G. Fang, J. Wu, H. Wang, R. Zhang, S. Kaneko, J. Zheng, H. Wang, D. Li, *Appl. Surf. Sci.* **2015**, *331*, 309.
- [23] H. Liu, J. Wang, X. Zhang, D. Zhou, X. Qi, B. Qiu, J. Fang, R. Kloepsch, G. Schumacher, Z. Liu, J. Li, *ACS Appl. Mater. Interfaces* **2016**, *8*, 4661.
- [24] B. Zong, Y. Lang, S. Yan, Z. Deng, J. Gong, J. Guo, L. Wang, G. Liang, *Mater. Today Commun.* **2020**, *24*, 101003.
- [25] C.-T. Chu, A. Mondal, N. V. Kosova, J.-Y. Lin, *Appl. Surf. Sci.* **2020**, *530*, 147169.
- [26] D. S. Lu, L. B. Yuan, J. L. Li, R. Q. Huang, J. H. Guo, Y. P. Cai, *J. Electroanal. Chem.* **2015**, *758*, 33.
- [27] N. P. W. Pieczonka, Z. Liu, P. Lu, K. L. Olson, J. Moote, B. R. Powell, J. H. Kim, *J. Phys. Chem. C* **2013**, *117*, 15947.
- [28] Y. Chen, Y. Sun, X. Huang, *Comput. Mater. Sci.* **2016**, *115*, 109.
- [29] W. Zhu, D. Liu, J. Trottier, C. Gagnon, J. Howe, A. Mauger, C. M. Julien, K. Zaghib, *J. Power Sources* **2015**, *298*, 341.
- [30] Y. Xue, Z. Wang, F. Yu, Y. Zhang, G. Yin, *J. Mater. Chem. A* **2014**, *2*, 4185.
- [31] W. K. Pang, H.-F. Lin, V. K. Peterson, C.-Z. Lu, C.-E. Liu, S.-C. Liao, J.-M. Chen, *J. Phys. Chem. C* **2017**, *121*, 3680.
- [32] K. R. Chemelewski, D. W. Shin, W. Li, A. Manthiram, *J. Mater. Chem. A* **2013**, *1*, 3347.
- [33] X. Feng, C. Shen, X. Fang, C. Chen, *Chin. Sci. Bull.* **2012**, *57*, 4176.
- [34] J. Zheng, J. Xiao, X. Yu, L. Kovarik, M. Gu, F. Omenya, X. Chen, X.-Q. Yang, J. Liu, G. L. Graff, M. S. Whittingham, J.-G. Zhang, *Phys. Chem. Chem. Phys.* **2012**, *14*, 13515.
- [35] S. Nageswaran, M. Keppeler, S.-J. Kim, M. Srinivasan, *J. Power Sources* **2017**, *346*, 89.
- [36] T.-F. Yi, Y. Xie, Y.-R. Zhu, R.-S. Zhu, M.-F. Ye, *J. Power Sources* **2012**, *217*, 59.
- [37] H.-G. Jung, M. W. Jang, J. Hassoun, Y.-K. Sun, B. Scrosati, *Nat. Commun.* **2011**, *2*, 516.
- [38] U. Nisar, R. Amin, R. Essehli, R. A. Shakoor, R. Kahraman, D. K. Kim, M. A. Khaleel, I. Belharouak, *J. Power Sources* **2018**, *396*, 774.
- [39] J. Liu, Z. Sun, J. Xie, H. Chen, N. Wu, B. Wu, *J. Power Sources* **2013**, *240*, 95.
- [40] K. R. Chemelewski, A. Manthiram, *J. Phys. Chem. C* **2013**, *117*, 12465.
- [41] W. Zhu, D. Liu, J. Trottier, C. Gagnon, A. Guerfi, C. M. Julien, A. Mauger, K. Zaghib, *J. Power Sources* **2014**, *264*, 290.
- [42] S. R. Li, C. H. Chen, J. R. Dahn, *J. Electrochem. Soc.* **2013**, *160*, 2166.
- [43] M. Kim, Y. Lee, T. Kiet, J. Inn, K. Park, *Appl. Surf. Sci.* **2020**, *504*, 144514.
- [44] J. Molenda, *Solid State Ionics* **2004**, *171*, 215.
- [45] M.-C. Yang, B. Xu, J.-H. Cheng, C.-J. Pan, B.-J. Hwang, Y. S. Meng, *Chem. Mater.* **2011**, *23*, 2832.
- [46] A. Milewska, Ł. Kondracki, M. Molenda, M. Bakierska, J. Molenda, *Solid State Ionics* **2014**, *267*, 27.
- [47] G. B. Zhong, Y. Y. Wang, X. J. Zhao, Q. S. Wang, Y. Yu, C. H. Chen, *J. Power Sources* **2012**, *216*, 368.
- [48] Y. Luo, T. Lu, Y. Zhang, L. Yan, S. S. Mao, J. Xie, *J. Alloys Compd.* **2017**, *703*, 289.

- [49] S. Li, Y. Wei, P. Wang, Y. Feng, W. Liang, H. Ding, X. Cui, *J. Alloys Compd.* **2020**, *820*, 153140.
- [50] O. Sha, Z. Tang, S. Wang, W. Yuan, Z. Qiao, Q. Xu, L. Ma, *Electrochim. Acta* **2012**, *77*, 250.
- [51] B. León, J. M. Lloris, C. P. Vicente, J. L. Tirado, *Electrochem. Solid-State Lett.* **2006**, *9*, 96.
- [52] J. Deng, Y. Xu, L. Xiong, L. Li, X. Sun, Y. Zhang, *J. Alloys Compd.* **2016**, *677*, 18.
- [53] S.-T. Myung, S. Komaba, N. Kumagai, H. Yashiro, H.-T. Chung, T.-H. Cho, *Electrochim. Acta* **2002**, *47*, 2543.
- [54] S.-H. Park, Y.-K. Sun, *Electrochim. Acta* **2004**, *50*, 439.
- [55] E. Zhao, L. Wei, Y. Guo, Y. Xu, W. Yan, D. Sun, Y. Jin, *J. Alloys Compd.* **2017**, *695*, 3393.
- [56] H. Duncan, Y. Abu-Lebdeh, I. J. Davidson, *J. Electrochem. Soc.* **2010**, *157*, 528.
- [57] J. Wang, W. Lin, B. Wu, J. Zhao, *J. Mater. Chem. A* **2014**, *2*, 16434.
- [58] H. Luo, P. Nie, L. Shen, H. Li, H. Deng, Y. Zhu, X. Zhang, *ChemElectroChem* **2015**, *2*, 127.
- [59] Y. Xiao, W. Xiang, J. Zhang, Y. Zhu, X. Guo, *Ionics* **2016**, *22*, 1361.
- [60] U. Jeong, Y. Yin, *Adv. Funct. Mater.* **2020**, *30*, 1907059.
- [61] Z. Liu, Y. Jiang, X. Zeng, G. Xiao, H. Song, S. Liao, *J. Power Sources* **2014**, *247*, 437.
- [62] M. Jagtoyen, F. Derbyshire, *Carbon* **1998**, *36*, 1085.
- [63] J. Hassoun, P. Reale, S. Panero, B. Scrosati, *Isr. J. Chem.* **2008**, *48*, 229.
- [64] S. Wei, D. Di Lecce, R. Messini D'Agostini, J. Hassoun, *ACS Appl. Energy Mater.* **2021**, *4*, 8340.
- [65] B. Boukamp, *Solid State Ionics* **1986**, *18–19*, 136.
- [66] B. Boukamp, *Solid State Ionics* **1986**, *20*, 31.
- [67] Y. Wang, Z. Ma, C. Lu, *Compos. Interfaces* **2016**, *23*, 273.
- [68] G. A. Elia, F. Nobili, R. Tossici, R. Marassi, A. Savoini, S. Panero, J. Hassoun, *J. Power Sources* **2015**, *275*, 227.
- [69] S. Wei, D. Di Lecce, J. Hassoun, *J. Electrochem. Soc.* **2021**, *168*, 030537.
- [70] D. Di Lecce, D. Campanella, J. Hassoun, *J. Phys. Chem. C* **2018**, *122*, 23925.
- [71] T. Peng, W. Guo, C. Liu, Y. Zhang, Y. Wang, Y. Guo, D. Zhang, H. Yan, Y. Lu, Y. Luo, *J. Solid State Electrochem.* **2019**, *23*, 2927.
- [72] M. Mo, K. S. Hui, X. Hong, J. Guo, C. Ye, A. Li, N. Hu, Z. Huang, J. Jiang, J. Liang, H. Chen, *Appl. Surf. Sci.* **2014**, *290*, 412.
- [73] O. Tiurin, N. Solomatin, M. Auinat, Y. Ein-eli, *J. Power Sources* **2020**, *448*, 227373.
- [74] Y.-F. Deng, S.-X. Zhao, Y.-H. Xu, K. Gao, C.-W. Nan, *Chem. Mater.* **2015**, *27*, 7734.
- [75] D. W. Shin, C. A. Bridges, A. Huq, M. P. Paranthaman, A. Manthiram, *Chem. Mater.* **2012**, *24*, 3720.
- [76] R. Verrelli, B. Scrosati, Y. Sun, J. Hassoun, *ACS Appl. Mater. Interfaces* **2014**, *6*, 5206.
- [77] J.-S. Bridel, S. Grugeon, S. Laruelle, J. Hassoun, P. Reale, B. Scrosati, J.-M. Tarascon, *J. Power Sources* **2010**, *195*, 2036.